Fluidic Assembly and Packing of Microspheres in Confined Channels

Siva A. Vanapalli,[†,‡] Christopher R. Iacovella,[†,‡] Kyung Eun Sung,[†] Deshpremy Mukhija,[†] Joanna M. Millunchick,[§] Mark A. Burns,[†,||] Sharon C. Glotzer,[†,§] and Michael J. Solomon*[,†]

Department of Chemical Engineering, Department of Materials Science and Engineering, and Department of Biomedical Engineering, University of Michigan, Ann Arbor, Michigan 48109

Received December 9, 2007

We study fluidic assembly and packing of spherical particles in rectilinear microchannels that are terminated by a flow constriction. First, we introduce a method for active assembly of particles in the confined microchannels by triggering a local constriction in the fluid channel using a partially closed membrane valve. This microfluidic valve allows active, on-demand particle assembly as opposed to previous passive assembly methods based on terminal channels and weirs. Second, we study the three-dimensional assembly and packing of particles against a weir in confined rectilinear microchannels. The packings result in achiral particle chains with alternating (zigzag) structure. This structure is characterized by a single, repeated bond angle whose components projected into the frame of the channel are quantified by confocal microscopy and image processing. Brownian dynamics simulation of the packing comprehensively delineates the range of bond angles possible in narrow, rectilinear microchannels as well as the complex dependence of these angles on the relative dimensions of the channel and particles. The simulations of the three-dimensional packings are accurately modeled by a compact theory based on trigonometric relationships. The experimentally measured bond angles show excellent agreement with the simulations, thereby validating the functional dependence of the achiral packing bond angles on channel dimensions. This functional relationship is immediately useful for the design of anisotropic particles by microfluidic synthesis.

I. Introduction

Particles with a range of anisotropies and length scales have been synthesized to date.[1] For applications driven by self-assembly, such as photonics, anisotropic particles with directional interactions are most useful.[2−6] For example, to build a photonic structure with diamond symmetry, anisotropic nanocolloids with tetrahedral attractive interactions are desirable.[2,5] Alternatively, anisotropic particles including non-Brownian particles find application in biosensing[7,8] and drug delivery.[9,10] For example, dot and stripe patterned rod-shaped particles (∼100 μm in size) have been used to detect biomolecules,[7,8] and shape anisotropy has been shown to impact the efficiency of particle phagocytosis by living cells.[9,10] Among the recent approaches[11−24] to synthesize anisotropic particles, microfluidics has emerged as a promising tool for continuous synthesis. Current microfluidic methods use droplet-[25−30] and mask-based photopolymerization[31,32] to synthesize anisotropic particles. Although these methods provide high throughput capability and good particle shape control, they are limited in incorporating complex chemical and material anisotropy, since the method relies on solidification of liquid precursors.

Recently, we introduced a microfluidic technique where encoded particle sequences are packed and bonded together in confined geometries to yield structures of both varied material and shape anisotropy.[33] Figure 1 illustrates this microfluidic approach, where programmable fluid flow is used to pack

* Corresponding author: E-mail: mjsolo@umich.edu.
† Department of Chemical Engineering.
‡ These two authors contributed equally.
§ Department of Materials Science.
|| Department of Biomedical Engineering.

(1) Glotzer, S. C.; Solomon, M. J. *Nat. Mater.* **2007**, *6*, 557−562.
(2) van Blaaderen, A. *Nature* **2006**, *439*, 545−546.
(3) Velikov, K. P.; van Dillen, T.; Polman, A.; van Blaaderen, A. *Appl. Phys. Lett.* **2002**, *81*, 838−840.
(4) Lu, Y.; Yin, Y.; Xia, Y. A. *Adv. Mater.* **2001**, *13*, 415−420.
(5) Zhang, Z. L.; Keys, A. S.; Chen, T.; Glotzer, S. C. *Langmuir* **2005**, *21*, 11547−11551.
(6) Maldovan, M.; Thomas, E. L. *Nat. Mater.* **2004**, *3*, 593−600.
(7) Pregibon, D. C.; Toner, M.; Doyle, P. S. *Science* **2007**, *315*, 1393−1396.
(8) Braeckmans, K.; De Smedt, S. C.; Leblans, M.; Pauwels, R.; Demeester, J. *Nat. Rev. Drug Discovery* **2002**, **1**, 447−456.
(9) Geng, Y.; Dalhaimer, P.; Cai, S.; Tsai, R.; Tewari, M.; Minko, T.; Discher, D. E. *Nat. Nanotechnol.* **2007**, *2*, 249−255.
(10) Champion, J. A.; Mitragotri, S. *Proc. Natl. Acad. Sci. U.S.A.* **2006**, *103*, 4930−4934.
(11) Furst, E. M.; Suzuki, C.; Fermigier, M.; Gast, A. P. *Langmuir* **1998**, *14*, 7334−7336.
(12) Yin, Y.; Lu, Y.; Gates, B.; Xia, Y. *J. Am. Chem. Soc.* **2001**, *2001*, 8718−8729.
(13) Terray, A.; Oakey, J.; Marr, D. W. M. *Appl. Phys. Lett.* **2002**, *81*, 1555−1557.
(14) Cayre, O.; Paunov, V. N.; Velev, O. D. *J. Mater. Chem.* **2003**, *13*, 2445−2450.
(15) Lu, Y.; Xiong, H.; Jiang, X. C.; Xia, Y. N.; Prentiss, M.; Whitesides, G. M. *J. Am. Chem. Soc.* **2003**, *125*, 12724−12725.
(16) Manoharan, V. N.; Elsesser, M. T.; Pine, D. J. *Science* **2003**, *301*, 483−487.
(17) Cho, Y. S.; Yi, G. R.; Lim, J. M.; Kim, S. H.; Manoharan, V. N.; Pine, D. J.; Yang, S. M. *J. Am. Chem. Soc.* **2005**, *127*, 15968−15975.
(18) Millman, J. R.; Bhatt, K. H.; Prevo, B. G.; Velev, O. D. *Nat. Mater.* **2005**, *4*, 98.
(19) Rolland, J. P.; et al. *J. Am. Chem. Soc.* **2005**, *127*, 10096−10100.
(20) Roh, K. H.; Martin, D. C.; Lahann, J. *Nat. Mater.* **2005**, *4*, 759−763.
(21) Snyder, C. E.; Yake, A. M.; Feick, J. D.; Velegol, D.; *Langmuir* **2005**, *21*, 4813−4815.
(22) Valignat, M. P.; Theodoly, O.; Crocker, J. C.; Russel, W. B.; Chaikin, P. M. *Proc. Nat. Acad. Sci.U.S.A.* **2005**, *102*, 4225−4229.
(23) Zhang, G.; Wang, D. Y.; Mohwald, H. *Angew. Chem., Int. Ed.* **2005**, *44*, 7767−7770.
(24) Hong, L.; Jiang, S.; Granick, S. *Langmuir* **2006**, *22*, 9495−9499.
(25) Nisisako, T.; Torii, T.; Higuchi, T. *Chem. Eng. J.* **2004**, *101*, 23−29.
(26) Dendukuri, D.; Tsoi, K.; Hatton, T. A.; Doyle, P. S. *Langmuir* **2005**, *21*, 2113−2116.
(27) Fernandez-Nieves, A.; Cristobal, G.; Garces-Chavez, V.; Spalding, G. C.; Dholakia, K.; Weitz, D. A. *Adv. Mater.* **2005**, *17*, 680−684.
(28) Nie, Z. H.; Xu, S. Q.; Seo, M.; Lewis, P. C.; Kumacheva, E. *J. Am. Chem. Soc.* **2005**, *127*, 8058−8063.
(29) Xu, S.; Nie, Z.; Seo, M.; Lewis, P.; Kumacheva, E.; Stone, H. A.; Garstecki, P.; Weibel, D. B.; Gitlin, I.; Whitesides, G. M. *Angew. Chem., Int. Ed.* **2005**, *44*, 724−728.
(30) Shepherd, R. F.; Conrad, J. C.; Rhodes, S. K.; Link, D. R.; Marquez, M.; Weitz, D. A.; Lewis, J. A. *Langmuir* **2006**, *22*, 8618−8622.
(31) Dendukuri, D.; Pregibon, D. C.; Collins, J.; Hatton, T. A.; Doyle, P. S. *Nat. Mater.* **2006**, *5*, 365−369.
(32) Dendukuri, D.; Gu, S. S.; Pregibon, D. C.; Hatton, T. A.; Doyle, P. S. *Lab Chip* **2007**, *7*, 818−828.

10.1021/la703840w CCC: $40.75
Published on Web 02/23/2008

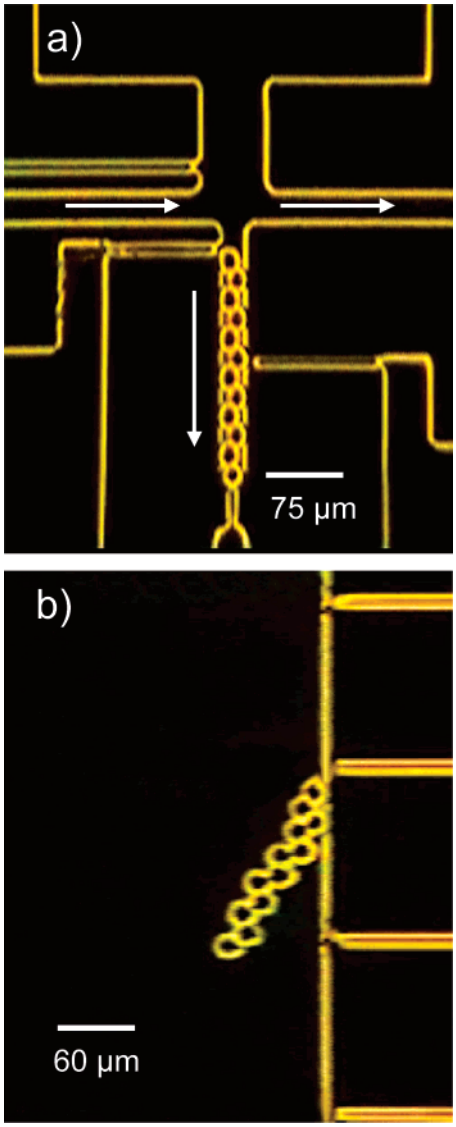

Figure 1. Anisotropic particle synthesis by fluidic assembly of microspheres (of diameter 21 μm) in confined microchannels. (a) Fluidic device showing packing of particles in a confined channel (width × height = 25 × 25 μm^2) by programmable fluid flow. The arrows show the direction of fluid flow. (b) Assembled microspheres in the terminal channel are fused (by heating at 80 °C) and the flow reversed to release the anisotropic particle into the reservoir. The length of the particle chain is ≈240 μm. For details of the synthesis method, see ref 33.

precursor polymeric spheres in a confined channel containing a terminal constriction (weir). The assembled spheres are fused by heating them near their glass transition temperature, and subsequently, the anisotropic particle chain with zigzag morphology is released by reversing the fluid flow.

In this study, we focus on two aspects that are relevant to the above fluidic approach for particle assembly and synthesis. First, unlike our prior use of passive structures such as weirs (cf. Figure 1) to assemble particles, here we develop a partially closed membrane valve that facilitates on-demand dynamic particle assembly in microchannels. These valves are amenable to fast actuation and parallelization lending the capability to increase the throughput of the anisotropic particle synthesis. Second, we provide design rules to determine particle packing and orientation in 3D microfluidic channels. Currently, it is possible to predict sphere packing under 2D confinement,[34] and in our previous work, we exploited this knowledge to synthesize anisotropic structures. However, execution of anisotropic particle synthesis (as described by the method in Figure 1) is preferred in 3D rather than 2D microfluidic channels because of (i) lower pressure drop and tolerance of particle polydispersity, (ii) relaxed tolerances on microfabrication, and (iii) the capability to process a range of particle sizes in the same device. Thus, particle packing in 3D geometries is most suitable for anisotropic particle synthesis, and to date, neither experimental nor theoretical studies have reported sphere packings in 3D rectangular geometries. Here we investigate with both experiment and simulation the three-dimensional orientation of individual spherical particles in confined 3D microchannels. In particular, we explore the phase space in channel geometry that yields anisotropic structures with zigzag morphology.

II. Materials and Methods

II.A. Fabrication and Characterization of Valve-Based Fluidic Devices. The fluidic devices were fabricated in polydimethoxysilane (PDMS) using multilayer soft lithography.[35] The molds for fluidic and control channels were made using SU-8 2025 and SU-8 2050, respectively. The nominal height of fluidic and control channels were 22 and 50 μm, respectively. The control channel was prepared by curing at 80 °C for 1 h a 10:1 ratio mixture of PDMS prepolymer and curing agent (Sylgard 184, Dow Corning, Midland, MI). Individual control channel devices were then cut using a scalpel and holes were punched. A 30:1 PDMS mixture was spin-coated on the wafer containing the fluidic channels and cured at 80 °C for 15 min. The control channel was aligned and placed on the partially cured fluidic channel and left overnight in the oven at 80 °C. The composite device was peeled from the wafer; holes were punched in the fluidic channel and sealed to glass cover slips using UV ozone (UVO cleaner, Jelight, Irvine, CA).

As a first step in addressing the capability of the partially closed membrane valve for particle assembly, we characterized membrane deformation in fluid channels that are close to square in cross-section. We directly visualized the three-dimensional deformation of the valve in the multilayer device using confocal microscopy. Figure 2a shows the cross-sectional confocal images of a multilayer fluidic device consisting of a fluid channel of width and height ($w \times h$) = 21.4 × 23.8 μm, control channel of $w \times h$ = 110 × 50 μm^2, and membrane thickness (δ) =30 μm. All the images shown in Figure 2 were taken along the central axis of the region, where the fluid and control channels overlap, without any pressure being imposed at the inlet of the fluid channel. Qualitatively, when the control channel is pressurized, we observe that initially the membrane deforms, leading to a decrease in the height of the fluid channel (Figure 2b). With further increase in pressure in the control channel, the height of the fluid channel continues to decrease and also we observe buckling in the sidewalls of the fluid channel. In particular, we find the onset of deformation in the sidewalls to occur at ~14 psi. When we increase the membrane thickness to 46 μm, keeping $w/h \approx 1$, we find that the sidewalls do not buckle even at control channel pressures of 20 psi (data not shown). This observed deformation of both the membrane and fluid channel in square channels is in contrast with that seen in wider rectangular channels[36] and has not been previously reported. The buckling effect can be mitigated by the use of thinner membranes; however, such membranes are prone to rupture due to defects introduced by dust particles.

We quantify the extent of deformation of the fluid channel as a function of applied pressure in Figure 2c for two devices that have $w/h \approx 1$ and membrane thickness of 30 and 47 μm. We defined the

(33) Sung, K. E.; Vanapalli, S. A.; Mukhija, D.; McKay, H. A.; Millunchick, J. M.; Burns, M. A.; Solomon, M. J. *J. Am. Chem. Soc.* **2008**, *130*, 1335−1340.

(34) Kumacheva, E.; Garstecki, P.; Wu, H.; Whitesides, G. M. *Phys. Rev. Lett.* **2003**, *91*, 128301.

(35) Unger, M. A.; Chou, H. P.; Thorsen, T.; Scherer, A.; Quake, S. R., *Science* **2002**, *288*, 113−116.

(36) Hoffman, J. M.; Shao, J.; Hsu, C. H.; Folch, A. *Adv. Mater.* **2004**, *16*, 2201−2206.

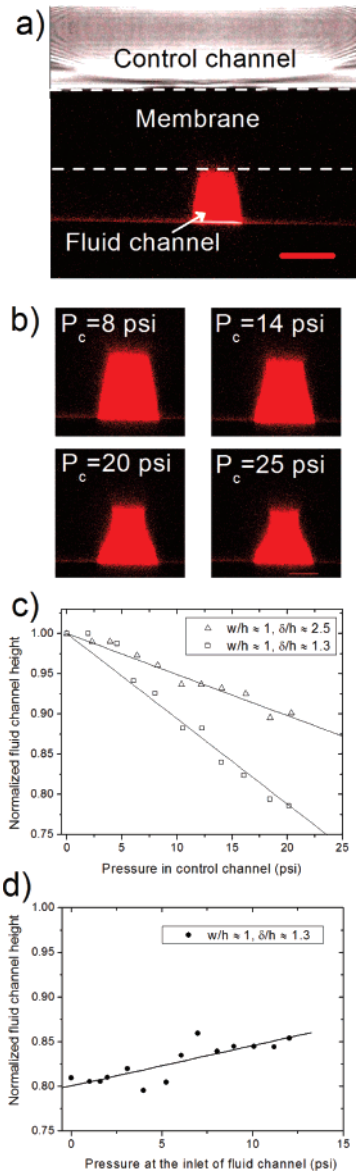

Figure 2. Characterization of the partially closed membrane valves. (a) Confocal cross-section image showing the fluid channel (w = 22 μm, h = 24 μm), control channel, and the membrane (δ = 30 μm). The region bounded by the dashed lines represents the membrane. (b) Deformation of the fluid channel at various control channel pressures. (c) Quantification of the fluid channel deformation as a function of control channel pressure for two different values of membrane thickness. During these measurements, the flow in the fluid channel was negligible. (d) Fluid channel deformation when the control channel was pressurized to 19 psi and the driving pressure at the inlet of the fluid channel was gradually varied. The scale bar in part a is 20 μm and that in part b is 10 μm.

normalized fluid channel height as the ratio of the heights of the fluid channel with and without the application of control channel pressure. Figure 2c shows that the normalized fluid channel height decreases linearly with applied pressure for both the devices. Given a particle size, the result of Figure 2c suggests that the local constriction in the fluid channel can be correspondingly tuned to impede particle flow, simply by pressure actuation.

The data in Figure 2c was generated without any driving pressure in the fluid channel. In Figure 2d, we report the effect of fluid flow on the normalized fluid channel height when the control channel was pressurized to 19 psi. The data show that the opening of the fluid channel remains partially closed with modest linear increase in normalized fluid channel height from ≈0.80 to ≈0.85 in the pressure range investigated here. This result suggests that this type of membrane valve is effective in arresting particle flow, even during strong fluid flow, due to the persistence of the constriction in the fluid channel.

II.B. Fabrication of Weir-Based Fluidic Devices. Silicon molds were used to cast weir-based fluidic devices in PDMS. The silicon molds were fabricated in the following way. Positive photoresist (PR 1827; Shipley Co., Newton, MA) was spun on a hexamethyldisilazane (HMDS; J.T. Baker, Phillipsburg, NJ) coated silicon wafer (⟨100⟩, 450 μm thick, 100 mm diameter). The wafer was soft-baked at 90 °C for 1 min, patterned by mask layer (clear field mask), developed in MF 319 solution (Rohm and Hass electronic materials, Spartanburg, SC) for 50 s, and hard-baked at 110 °C for 10 min in a convection oven. Then, the wafer was transferred into STS deep reactive ion etcher (Surface Technology System, Newport, UK) that uses alternating passivation (C_4F_8) and etching steps (SF_6 and O_2). After etching, the remaining photoresist was stripped in PRS 2000 solution (J.T. Baker, Phillipsburg, NJ). Finally, the wafer was rinsed in deionized water and air-dried.

II.C. Particle Assembly Experiments. The following procedure was used to generate particle assemblies using partially closed membrane valves. A dilute solution (0.05 wt %) of polystyrene particles of manufacturer reported diameter $\sigma = 21.14 \pm 0.04$ μm (Polysciences, Warrington, PA) was loaded into pressurized syringes and delivered into the fluidic channels of the multilayer device. Subsequently, the control channels were pressurized and actuated via a computer-controlled three-way solenoid valve. Images were acquired using a CCD camera (Cascade 512F, Roper Scientific) coupled to a Nikon TE200 inverted microscope.

To investigate the assembly of constituent particles in confined microchannels with weirs, the following device geometry was incorporated on the silicon mold (see Figure 3a). It consisted of a main fluidic channel (of width 50 μm) with side channels of varying width, each of which contained a weir (10 μm width). Five different channel aspect ratios were chosen to study particle packing (see Table 1). To pack the particles in side channels containing the weir, a bead solution admixed with fluorescein was injected at the inlet of the main channel, while the outlet was temporarily blocked. Imaging of the resultant particle assembly was performed using a confocal microscope (Lieca TCS SP2, Lieca Microsystems, Wetlar, Germany). Approximately 50−100 z-slices (spaced 0.488 μm apart) such as those reported in Figure 3b were collected using a 63× oil immersion objective of numerical aperture 1.4. Each of the acquired images is of size 512 × 512 pixels and has a spatial resolution of 0.465 μm/pixel.

II.D. Simulation Model and Method. To model packing in a microchannel, we utilized the method of Brownian dynamics (BD). In this case, BD is used for two main reasons. First, finding agreement between flow-induced experiments of non-Brownian particles and simulations of Brownian particles will serve to bolster the assertion that the structure is dominated only by packing and to suggest that this experimental method is applicable at smaller length scales where particles are Brownian. Second, BD is an efficient thermostat for allowing simulations to be run in the *NVT* ensemble that has been found to work well in small, confined systems.[37]

In BD each particle is subjected to conservative, frictional, and random forces $\mathbf{F}_i^C$, $\mathbf{F}_i^F$, and $\mathbf{F}_i^R$, respectively, and its trajectory obeys the Langevin equation[38] $(m_i)(a_i) = \mathbf{F}_i^C + \mathbf{F}_i^F + \mathbf{F}_i^R$. Since the random and frictional forces are not pairwise, momentum is not conserved and thus hydrodynamics is not included.[38] Particle−particle interactions are modeled by a soft potential

$$U(r) = \epsilon\left(1 + \cos\left(\frac{\pi r}{r_{cutoff}}\right)\right) \quad r < r_{cutoff} \tag{1}$$

where ϵ is the characteristic energy [$U(r) = 2\epsilon$ at $r = 0$] and r_{cutoff} is set to the particle diameter σ. This potential form was chosen because as ϵ increases, or similarly as temperature is decreased, the

(37) Iacovella, C. R.; Keys, A. S.; Horsch, M. A.; Glotzer, S. C. *Phys. Rev. E* **2007**, *75*, 040801.
(38) Grest, G. S.; Kremer, K. *Phys. Rev. A* **1986**, *33*, 3628−3631.

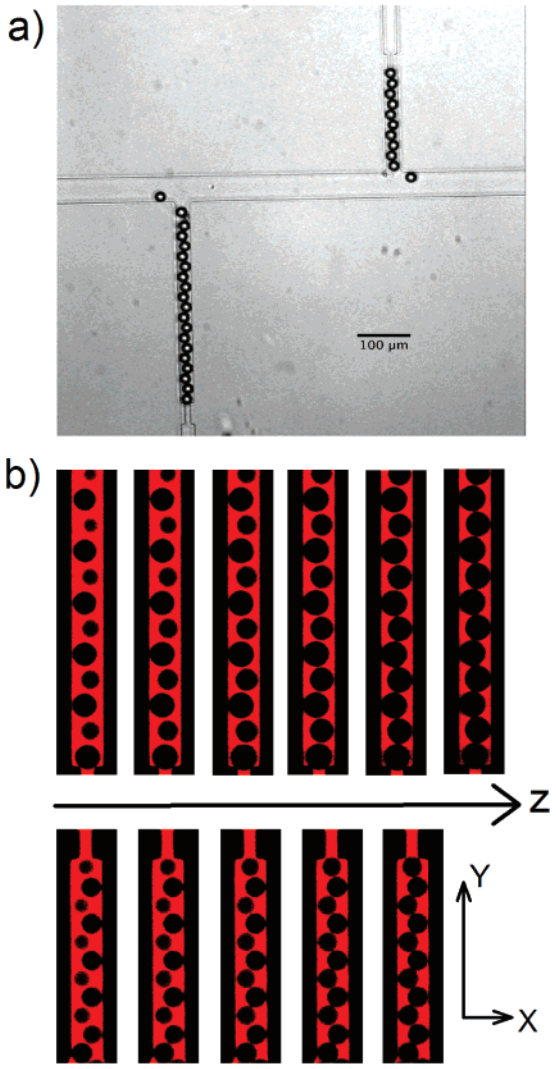

Figure 3. (a) Bright-field optical image showing the device geometry used to study the three-dimensional assembly and packing of spherical particles in confined microfluidic channels. (b) Direct visualization of the 3D assembly and packing in confined microchannels using confocal microscopy. A series of 2D confocal slices with cuts made at an increasing distance from the coverglass, spaced at 0.976 μm, showing the evolution of the assembly as a function of *z*-height (indicated by the arrow labeled *z*). The top series of images are for G2 geometry ($w = 25\,\mu$m, $h = 25\,\mu$m, $\sigma = 21.1\,\mu$m) and the bottom series are for G4 geometry ($w = 30\,\mu$m, $h = 30\,\mu$m, $\sigma = 21.1\,\mu$m).

Table 1. The Experimental Confined Channel Geometries Used To Assess the Assembly and Packing of Spherical Particles[a]

geometry	w (μm)	h (μm)	w/σ	h/σ	aspect ratio
G1	23	25	1.088	1.183	0.920
G2	25	25	1.183	1.183	1.000
G3	25	35	1.183	1.656	0.714
G4	30	30	1.419	1.419	1.000
G5	30	35	1.419	1.656	0.857

[a] The channel dimensions reported here correspond to design dimensions on the mask used for photolithography.

potential begins to closely approximate the hard sphere potential, capturing only excluded volume interactions. Since the polydispersity of particles is low, the simulations do not incorporate variations in particle size. Because of the very steep potential used, the time step for integrating the equations of motion is set to 10^{-11}. Particles are kept within channels by implementing two types of walls. The first wall is a reflective wall, where particle velocities perpendicular to the wall are negated if a particle crosses the boundary. The second wall is modeled by the soft potential, where a particle starts interacting with the wall as soon as it crosses the boundary, creating an additional confining surface. System sizes were kept commensurate with experiment at between 10 and 20 particles. The system is started from a disordered configuration at $k_BT/\epsilon = 0.2$ and then incrementally cooled to $k_BT/\epsilon = 1.67 \times 10^{-5}$ over ~1 000 000 time steps. Approximately 100 different state points were simulated, where each state point was calculated by averaging together two to four simulation runs. All distance results are presented in dimensions scaled by the particle diameter, σ.

II.E. Bond Angle Analysis. Particle centroids were determined from the raw confocal images using Image J v 1.36b (National Institutes of Health). An edge detection routine was used to determine particle boundaries and thereby the particle centroid coordinates (x_i, y_i) and diameter (σ_i) in the imaging ($x-y$) plane. In some instances, when the edge detection routine was not able to detect the single particle boundaries due to close contact between either the particles or particle and wall, particle boundaries were identified manually.

To quantify the relative orientation of each sphere within a chain (see Figure 4), we define the two bond angles $\theta = \tan^{-1}(\Delta x/\Delta y)$ and $\phi = \tan^{-1}(\Delta z/\Delta y)$, as well as the relative orientation of spheres within the particle plane, $\alpha = \sin^{-1}(\sqrt{(\Delta x)^2+(\Delta z)^2}/\sqrt{(\Delta x)^2+(\Delta y)^2+(\Delta z)^2})$. Here Δx, Δy, and Δz are the distances between two neighboring particles (1, 2) along the width, length, and depth of the channel, respectively. Experimentally, we determine Δx as $x_1 - x_2$, Δy as $y_1 - y_2$ and Δz as $z_1 - z_2$, where $z_i = 1/2\sqrt{\sigma^2-\sigma_i^2}$. In determining the bond angles from both simulation and experiment, we define the diameter of the particle, σ, to be the average separation between neighboring particle positions, making the assumption that the system is close-packed and scale coordinates accordingly. The assumption of close-packed structures is supported by the confocal images of experiments and the nature of the flow-induced assembly, as discussed in the next section. Similarly, we calculate the actual width and height of the geometry (reported in Table 2) from the experimentally derived average position of the particles in the *x*- and *z*-directions and use this as input to the simulation studies. Note that in all cases channel aspect ratio is defined as width/height.

III. Results and Discussion

III.A. Microfluidic Valve for Particle Assembly. Quake and co-workers[35] introduced membrane valves that were fabricated using multilayer soft lithography. The valve functionality arises from the deformation of the thin membrane sandwiched between the fluid and control channels that are oriented perpendicular to each other. If the fluid channel cross-section is rounded, then it can be closed completely. Alternatively, if the cross-section is rectangular, then the fluid channels can be only partially closed.[35,39] To date, both types of valves have been principally used to control fluid flow in microfluidic devices. Here we fabricate polydimethylsiloxane (PDMS) based multilayer devices with rectilinear cross-section such that spherical particles can be captured and assembled due to the actuation of the valve. To our knowledge, this is the first application of such an on-chip microfluidic valve for active particle assembly. The use of a rectilinear microchannel cross section (as opposed to the hemispheric cross section of ref 35) is ideal for the particle assembly application, because it facilitates the trapping of particles while still allowing the suspending medium to pass through the valve. This arrangement allows for the production of packings at the constriction that are dense relative to particle concentrations elsewhere in the fluidic device.

Figure 5a illustrates the operation of the membrane valve to facilitate particle assembly. A particle solution is loaded into a

(39) Lam, E. W.; Cooksey, G. A.; Finlayson, B. A.; Folch, A. *Appl. Phys. Lett.* **2006**, *89*, 164105.

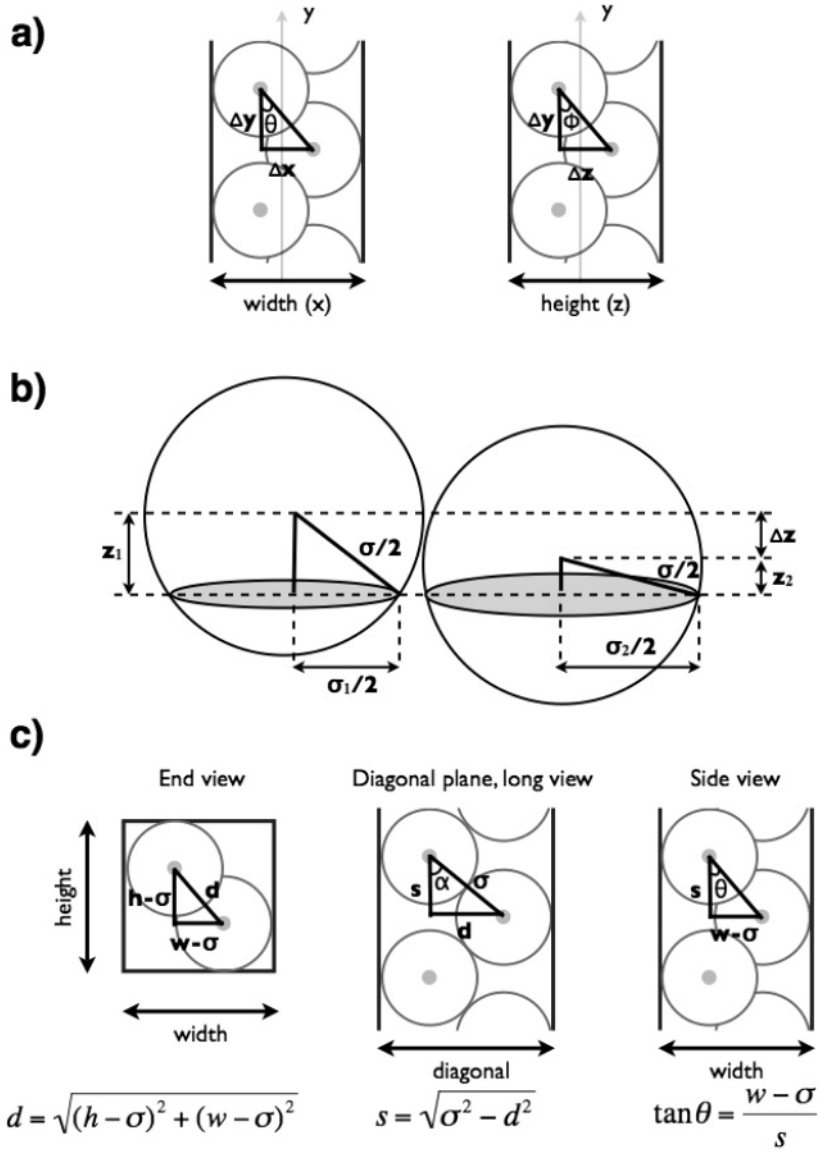

Figure 4. (a) A schematic representation of the definitions of the bond angles θ and ϕ used to characterize the zigzag particle chains. (b) A schematic illustrating the quantification of Δz from the confocal image slices (denoted in gray). (c) Definition of theoretical relation between particle orientation and height and width.

narrow fluid channel and the control channel is pressurized. The deflection of the membrane reduces the height of the fluid channel partially (see Figure 5b) and results in the capture of particles, while the fluid continues to flow. Figure 5c shows representative assemblies generated due to such an actuation of the membrane valve in confined channels. The microchannels generating these assemblies confine the particles in two dimensions. In such 2D channels, the relative orientation between the particles can be simply described by a single, repeating bond angle, α, where $\sin\alpha = (w/\sigma) - 1$ for $\alpha \lesssim 60°$.[34] For example, in the chains with zigzag structure, such as those in Figure 5, the experimentally measured α values are $2.6° \pm 2.3°$, $36.7° \pm 0.7°$, and $57.3° \pm 1.7°$, respectively. The corresponding values calculated from $\sin\alpha = (w/\sigma) - 1$ are in good agreement, specifically, 2.4°, 37.5°, and 53.8°. Previous experiments[33,40] with particle packing in similar, narrow 2D channels containing a weir are also consistent with this model, suggesting that for a given channel geometry both the membrane valve and the weir generate the same particle assembly. This equal performance of the two methods provides increased flexibility in the design of microfluidic platforms configured for synthesis of particular kinds of anisotropic particles.

III.B. Particle Assembly and Packing in Confined Microchannels—Experiments. Several experimental studies have exploited the packing of spheres in confined geometries to create novel assemblies. Assemblies of spherical particles have been generated by confining particles on the surface of emulsion droplets accompanied by evaporation-driven assembly.[16] Capillary flow-induced dewetting was used to confine particles in photolithographically defined geometric shapes to produce a variety of assemblies, including linear chains.[12] Flow-induced packing of particles against a constriction in channels has also been shown to be an effective means to generate novel assemblies.[34,40] In particular, Kumacheva and co-workers[34] studied flow-induced packing of particles against a weir in two-dimensionally confined microchannels of large aspect ratio [channel width (w)/particle diameter (σ) > 2] and observed the formation of 2D lattices of both hexagonal and rhombic symmetry. Similar to Kumacheva et al.,[34] we study flow-induced particle assembly; however, the results here build upon the earlier work in the following key ways. First, we focus on particle assembly

(40) Wu, H.; Thalladi, V. R.; Whitesides, S.; Whitesides, G. M. *J. Am. Chem. Soc.* **2002**, *124*, 14495−14502.

Table 2. Comparison of Packing Experiments, Simulation, and Theory[a]

	G1	G2	G3	G4	G5
width (exp)	1.14	1.21	1.21	1.46	1.40
width (sim)	1.14	1.21	1.21	1.47	1.40
height (exp)	1.22	1.20	1.51	1.23	1.63
height (sim)	1.23	1.20	1.51	1.23	1.63
aspect ratio (exp)	0.93	1.01	0.80	1.19	0.86
aspect ratio (sim)	0.93	1.01	0.80	1.20	0.86
θ (exp)	8.15 ± 1.11	12.42 ± 0.44	14.03 ± 0.58	28.49 ± 2.18	31.57 ± 0.22
θ (sim)	8.21 ± 0.01	12.56 ± 0.01	14.17 ± 0.34	28.74 ± 0.03	31.37 ± 0.36
θ (theory)	8.15	12.42	14.03	28.49	31.57
ϕ (exp)	13.13 ± 1.68	11.92 ± 1.87	31.28 ± 2.17	14.79 ± 1.16	43.93 ± 0.95
ϕ (sim)	13.23 ± 0.01	12.05 ± 0.01	31.33 ± 0.08	14.94 ± 0.02	43.86 ± 0.24
ϕ (theory)	13.13	11.92	31.28	14.79	43.93
v_f (exp)	0.39	0.38	0.34	0.34	0.35
v_f (sim)	0.39	0.38	0.34	0.34	0.35
v_f (theory)	0.39	0.38	0.34	0.34	0.35
α (exp)	15.31 ± 0.74	16.96 ± 0.60	33.30 ± 0.84	31.11 ± 0.54	48.81 ± 0.92
α (sim)	15.42 ± 0.02	17.15 ± 0.02	33.39 ± 0.16	31.38 ± 0.03	48.69 ± 0.27
α (theory)	15.31	16.96	33.30	31.11	48.81

[a] The errors are standard deviations.

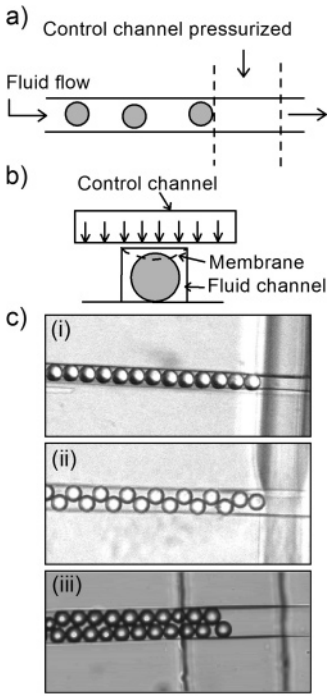

Figure 5. (a) Schematic of flow-induced assembly and packing of spherical particles using partially closed membrane valves (not drawn to scale). (b) Schematic cross-section of the valve showing the capture of the particle due to membrane deflection (shown by curved dashed line). (c) Representative assemblies generated by triggering the valve in confined channels of varied aspect ratios: (i) linear chain, $w = 22\ \mu$m, $h = 22\ \mu$m, $\delta = 21\ \mu$m, $\sigma = 21.1\ \mu$m; (ii) zigzag chain, $w = 34\ \mu$m, $h = 23\ \mu$m, $\delta = 37\ \mu$m, $\sigma = 21.1\ \mu$m; (iii) two-layer assembly, $w = 30\ \mu$m, $h = 22\ \mu$m, $\delta = 30\ \mu$m, $\sigma = 16.6\ \mu$m.

in confined channels of smaller diameter, i.e., $1 < w/\sigma < 1.86$, because the resulting chain structures are of interest for anisotropic particle synthesis. Second, by building packings with three-dimensional structure, we potentially expand the diversity of particle orientations achieved for larger microchannels. Third, the requirement of full confinement in one dimension required for 2D lattices places stringent practical limitations on microfabrication (e.g., channel height tolerances) and microfluidics (e.g., large pressure drops and increased potential for clogging due to particle polydispersity) that can be avoided by exploiting packing in three dimensions. However, in this case, good understanding of the packings that result in 3D is required so that particles with the desired anisotropic structure can indeed be produced given a particular device design.

To investigate the relative orientation of particles in 3D confined channels we packed particles against a weir using fluid flow in channels of varying aspect ratio (see Table 1) and imaged them using confocal microscopy. We find that all the particle assemblies listed in Table 1 form zigzag chains characterized by a single, alternating bond angle, α, in the plane incorporating particle centroids (see Figure 4c). That is, packings are achiral with a repeat distance of two particles. We also characterize this single bond angle by resolving its components in the frame of the rectilinear microchannel (as per Figure 4). Moreover, Table 2 shows that the 3D zigzag structure can be varied broadly by designing the channel dimensions, and the morphology of the packing structures can be varied from linear to zigzag (see section III.C. for more elaborate discussion). Similar zigzag packing structures have also been observed under cylindrical confinement for aspect ratios ≤ 1.866.[41]

To assess the quality of flow-induced packing in confined microchannels, we report the distributions of the measured bond angles for two representative geometries in Figure 6. We find that the probability distributions of both θ and ϕ exhibit a maximum, indicating a preferential ordering of the particle pairs. From these distributions, we compute mean bond angles and standard deviations for comparison with simulation and theory. Additionally, a certain degree of variation in the bond angles exists, as reflected in the widths of the peaks in the probability distributions. Note that because of the skewness in experimental distributions, the standard deviation is not the only relevant parameter needed to characterize these distributions. In general, we find that the variation in θ (bond angle in $x-y$ plane) is less than in ϕ (bond angle in $y-z$ plane), due to the poorer resolution in determining the z-coordinate of the centroid. We also identify the following sources that could contribute to the spread in the distributions. First, we fabricated the molds in silicon and cast the devices in PDMS. The standard lithography process yields a variation of $\pm 1\ \mu$m in the targeted channel dimensions, implying $\sim$4% variation in aspect ratio. Second, the shrinkage in PDMS during the curing process leads to $\sim$1% variation in channel size.[42] Third, the polydispersity of the particles in our experiments

(41) Pickett, G. T.; Gross, M.; Okuyama, H. *Phys. Rev. Lett.* **2000**, *85*, 3652−3655.
(42) Anderson, J. R.; Chiu, D. T.; Jackman, R. J.; Cherniavskaya, O.; McDonald, J. C.; Wu, H.; Whitesides, S. H.; Whitesides, G. M. *Anal. Chem.* **2000**, *72*, 3158−3164.

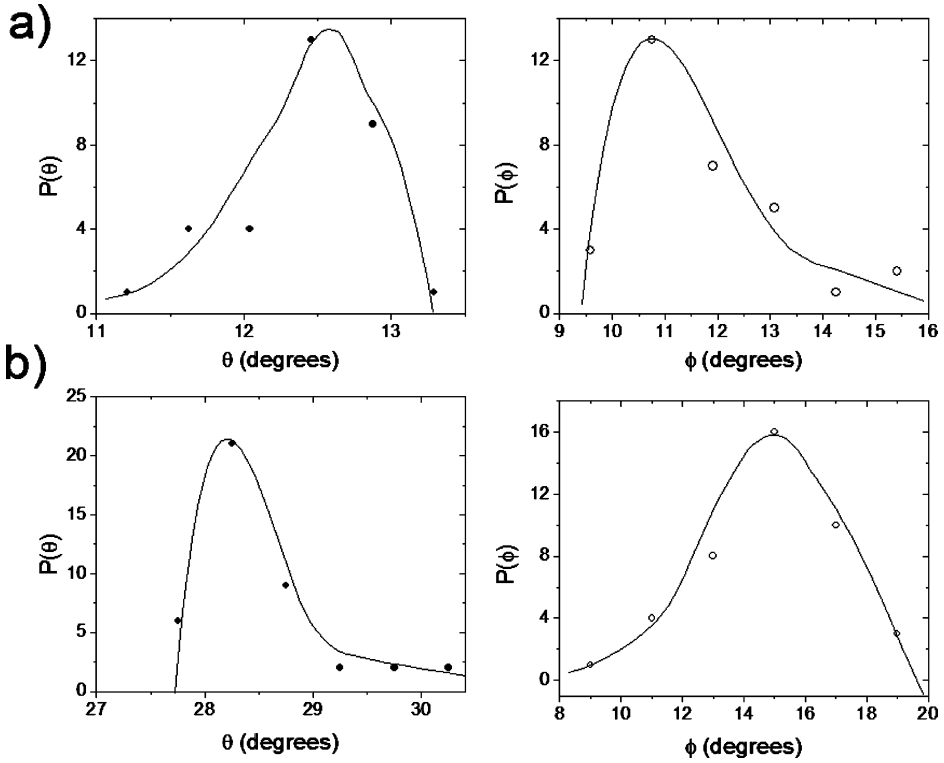

Figure 6. Experimentally determined probability distribution of the particle pair orientation angles θ and ϕ for the two representative geometries (a) G2 and (b) G4. The lines are drawn for clarity. Possible origins for the spread in the distributions are discussed in the text.

was measured to be ~3.5%. In spite of these nonidealities, the mean values of the bond angles, planar angle, and volume fraction are in excellent agreement with simulation and theory (see Table 2) as discussed in more detail in the following section.

III.C. Particle Assembly and Packing in Confined Microchannels—Simulations and Theory. Several simulation studies of confined particles in cylindrical domains that form close-packed structures[41,43,44] exist. However, there is little in the literature concerning confinement in the narrow rectilinear channels that are most useful for microfluidic synthesis. The Pickett et al.[41] study of particle confinement in small cylindrical domains is most relevant to this work, particularly in the range of channel diameters less than ~1.866, where zigzag morphologies were found. This paper builds upon and moves beyond the earlier work of Pickett et al. in three ways: (i) While Pickett et al. simulated packings in cylindrical geometry, this work addresses packing configurations in rectilinear channels. Because of their prevalence, rectilinear channels are of the greatest significance in microfluidics. (ii) This work tests packing simulations and theory by including a confocal microscopy study of the packings, thereby providing a link to experimental colloid science that is not made in Pickett et al. (iii) Since the work of Pickett et al. was concerned with chiral structures formed at diameters greater than 1.866, there was little analysis of achiral structures of zigzag morphology reported. In this work, we specifically investigate rectilinear cross-section microchannels where we expect achiral zigzag morphologies and investigate the specific impact these geometries have on volume fraction and the relative orientation between particles.

We conducted simulations at channel dimensions similar to those in our experiments. Figure 7 reports the simulated 3D renderings juxtaposed against the experimental images (confocal

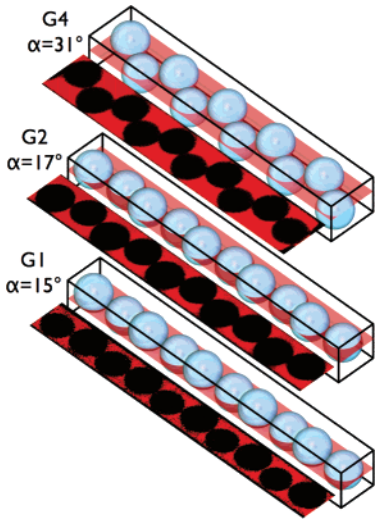

Figure 7. Comparison of experimental and simulated particle packings. The confocal slices (bottom) are shown corresponding to the cut made by the transparent plane in the simulated (top) 3D renderings for three channel geometries.

xy slices) for three of the channel geometries. Qualitatively, Figure 7 shows that the simulation and experiment are in good agreement, where structures vary from almost linear (G1) to strongly zigzag (G4). To compare with experiments, we extract θ, ϕ, and α from the simulated 3D structures and report them in Table 2. Overall, we find very good quantitative agreement with a very narrow distribution in θ, ϕ, and α, with a maximum standard deviation of less than 1°. The excellent agreement between experiment and simulation in these five cases suggests that Brownian motion is not important to the formation of these structures and our simulation method is appropriate for investigating the full range of structures.

Using simulation, we now comprehensively delineate the dependence of θ, ϕ, α, and volume fraction (v_f) on the height

(43) Gordillo, M. C.; Martinez-Haya, B.; Romero-Enrique, J. M. *J. Chem. Phys.* **2006**, *125*, 144702.
(44) Koga, K.; Tanaka, H. *J. Chem. Phys.* **2006**, *124*, 131103.

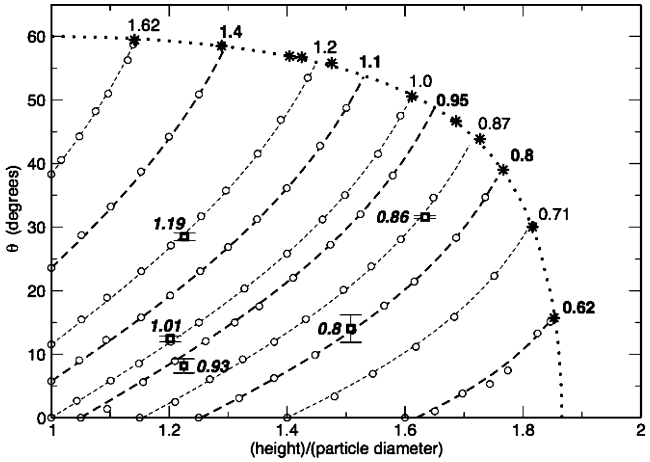

Figure 8. θ as a function of reduced channel height and aspect ratio. Squares represent experimental data points from Table 2 (aspect ratio labeled in italics), circles are simulated points, and dashed lines are theoretical calculations (eq 2). The dotted line that encompasses the data is the theoretically predicted phase boundary (eq 6) and stars represent the simulated points predicting the phase boundary. Aspect ratios (width/height) are labeled within the plot.

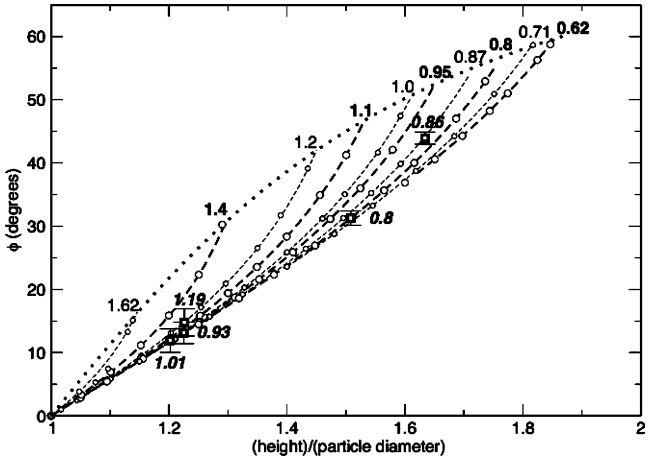

Figure 9. ϕ as a function of reduced channel height and aspect ratio. Squares represent experimental data points from Table 2 (aspect ratio labeled in italics), circles are simulated points, and dashed lines are theoretical calculations (eq 3). The dotted line that encompasses the data represents the theoretically determined phase boundary (eq 7). Aspect ratios (width/height) are labeled within the plot.

and width of the microchannel for structures that exhibit the zigzag morphology. These results are summarized in Figures 8−11, where in all cases we group the data by aspect ratio (w/h) and plot θ, ϕ, α, and υ_f as a function of reduced microchannel height for aspect ratios ranging from 0.62 to 1.62. Note that reduced microchannel dimensions are those distances scaled by particle diameter, σ. We observe from our simulations that close-packed structures are formed over the entire range and use this observation to develop a theoretical relationship for packing based on simple trigonometric relationships. Figure 4c summarizes the basic progression for determining these relationships based on height and width. The resulting relationships are

$$\theta = \tan^{-1}\left(\frac{w-\sigma}{\sqrt{\sigma^2 - [(h-\sigma)^2 + (w-\sigma)^2]}}\right) \quad (2)$$

$$\phi = \tan^{-1}\left(\frac{h-\sigma}{\sqrt{\sigma^2 - [(h-\sigma)^2 + (w-\sigma)^2]}}\right) \quad (3)$$

$$\alpha = \sin^{-1}\left(\frac{\sqrt{(h-\sigma)^2 + (w-\sigma)^2}}{\sigma}\right) \quad (4)$$

$$\upsilon_f = \frac{\sigma^3\pi/6}{hw(w-\sigma)/\tan(\theta)} \quad (5)$$

It is clear that for the 2D case, where $h = \sigma$, eq 4 will reduce to $\sin\alpha = (w/\sigma) - 1$, as given by Kumacheva et al.[34] These theoretical predictions appear as dotted and dashed lines in Figures 8−11, showing excellent agreement with simulation; these results also appear in Table 2, again showing excellent agreement with both simulation and experiment. Small deviations exist between simulation and theory in Figures 8−11, primarily as a result of variations in the actual aspect ratio calculated in the simulations. While the soft potential we use closely approximates the hard sphere potential, particles still can overlap a small amount, which can perturb the calculated height or width from the set values.

Figures 8 and 9 show the dependence of θ and ϕ on both reduced height and aspect ratio, where in all cases both angles increase as reduced height or aspect ratio are increased. It is important to note the bounding line that encompasses our data in Figures 8 and 9 predicts the phase boundary for the zigzag

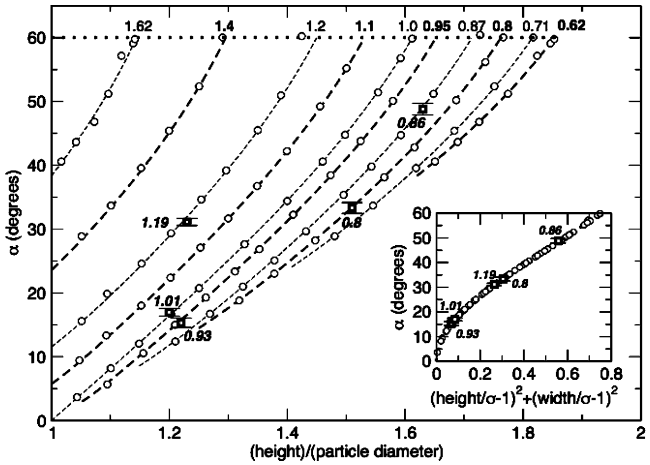

Figure 10. Planar angle (α) between particles as a function of reduced channel height and aspect ratio. Squares represent experimental data points from Table 2 (aspect ratio labeled in italics), circles are simulated points, and dashed lines are theoretical calculations (eq 4). The dotted line at $\alpha = 60°$ is the maximum achievable angle (i.e., phase boundary). Aspect ratios (width/height) are labeled within the plot. The inset plot shows the data from the main plot reduced to a single curve by plotting α vs $[(\text{height}/\sigma - 1)^2 + (\text{width}/\sigma - 1)^2]$.

morphology found via simulation and predicted with the theoretical relation (eqs 2 and 3). This phase boundary represents the transition from 2D planar zigzag structures oriented in a 3D channel to true 3D structures. To predict this phase boundary theoretically, the angle separating particles in the particle plane, α, is set to 60°, as defined in Figure 4c, corresponding to 2D hexagonal packing. At this condition all neighboring particles are touching and separated by σ; with this eqs 2 and 3 reduce to

$$\theta_{\text{boundary}} = \tan^{-1}\left(\frac{w-\sigma}{0.5\sigma}\right) \quad (6)$$

$$\phi_{\text{boundary}} = \tan^{-1}\left(\frac{h-\sigma}{0.5\sigma}\right) \quad (7)$$

Equations 6 and 7 are plotted as the phase boundaries in Figures 8 and 9, respectively.

Figure 10 predicts the dependence of the planar angle, α, on height and aspect ratio. Again, the transition from 2D planar

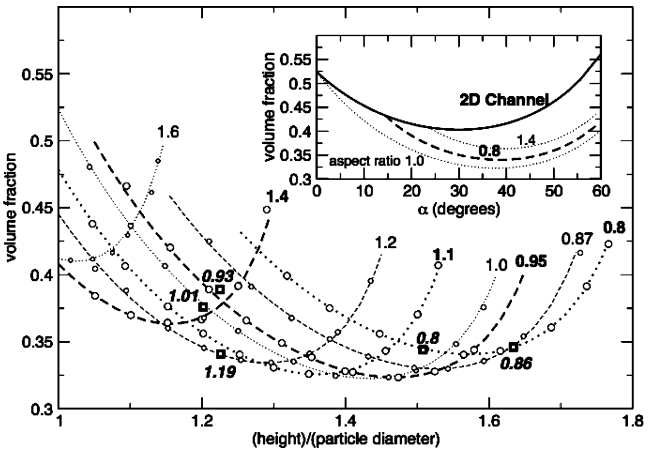

Figure 11. Particle volume fraction as a function of reduced channel height and aspect ratio. Squares represent experimental data points from Table 2 (aspect ratio labeled in italics), circles are simulated points, and dashed lines are theoretical calculations (eq 6). Aspect ratios (width/height) are labeled within the plot. The inset shows the comparative plot of volume fraction under 2D and 3D confinement.

morphologies to 3D structures occurs when all neighboring particles are touching, which corresponds to a planar angle of 60°. Thus, the phase boundary occurs as a straight line at $\alpha = 60°$ for all aspect ratios. The inset of Figure 10 shows that, consistent with eq 4, the data for the planar angle can be mapped onto a single curve by choosing the geometric length scale as $(h/\sigma - 1)^2 + (w/\sigma - 1)^2$. The planar angle is of particular interest, because it is the characteristic angle to describe the anisotropic particle that results from fusing the spheres and releasing them from the channel (cf. Figure 1). Figure 10 also highlights some of the advantages of creating these assemblies in 3D microchannels. It is clear that there are multiple combinations of reduced height and aspect ratio (and hence reduced width) that can give the same α value. Additionally, by changing the particle diameter, one can access a huge range of α values from the same channel. This is not the case when considering a 2D channel. If we decrease the size of the particle in a fixed 2D channel, the height would be greater than σ, and thus it would be necessary to treat it as packing in a 3D channel; in order to maintain the 2D relationship, it would be necessary to fabricate a new channel of height equal to σ.

In addition to the bond and planar angles reported in Figures 8−10, the microparticle concentration in the fluidic channel is of interest, because it is a principal determinant of the pressure drop required to flow fluid through the channel. Figure 11 shows the dependence of v_f on reduced height and aspect ratio, where aspect ratio ranges from 0.8 to 1.6. We again find excellent agreement between simulation and theory. It is interesting to note that, for each aspect ratio, the volume fraction curves show a minimum. This behavior can be understood intuitively by examining the available sphere packings. We have three basic sphere packings available; at one extreme particles pack into 2D hexagonally close-packed structures, at the other extreme particles pack into a straight line, and intermediate between these two extremes the zigzag morphology is formed. The 2D hexagonally close-packed structure will have the densest packing, with $v_f \sim 0.56$ for a system with height $= \sigma$. However, this volume fraction will decrease as we progress from asymmetric (rectangular) to symmetric (square) channels. This decrease is due to the fact that particles pack along the diagonal of the box, and while 2D hexagonal packing is the best within the plane of the particles, the amount of free volume above and below the plane increases as the channel becomes more symmetric. If we decrease the height or width in a system that exhibits hexagonal packing, we begin to adopt the zigzag morphology which increases the free space within the plane of the particles, thus decreasing the volume fraction. At the other extreme we have a perfect line, with $v_f \sim 0.52$ when the height $= \sigma$. If we increase the height or width for a fixed aspect ratio, we will begin to find the zigzag morphology, where particles have additional free space surrounding them, thus decreasing the volume fraction.

The inset of Figure 11 compares the dependence of volume fraction on planar angle α under 2D and 3D confinement. It is clear that for each value of α the volume fraction of the 3D system will always be less than that of the 2D system, with the exception of a single point. Thus, we anticipate that the particle packings in a 3D microchannel will incur less pressure drop than in a 2D channel, again where a 2D channel corresponds to the case where the height is equal to the particle diameter. It is also interesting to note that the volume fraction curves in 3D channels terminate at specific (low) values of α on the 2D channel volume fraction curve. This is because the ability to create weakly zigzag structures (e.g., a nearly straight chain, $\alpha \approx 0$) is lost when using wider aspect ratio channels that induce 3D confinement.

With the availability of the theoretical relationships we can now estimate the range of uncertainty in θ and ϕ, given a certain degree of uncertainty in experimental parameters. Note that experimental uncertainty in either the particle size or channel dimensions translates to a net uncertainty in aspect ratio. Therefore, if we assume that the uncertainty in the aspect ratio is within 2−5%, we find that for small values of height (those values below the midpoint of the accessible range for a specific aspect ratio), θ will deviate by ∼0.5−1°. However, for the larger accessible values of height, θ will deviate by at most ∼2.5−6.5°. Similarly, ϕ will deviate ∼2−4° for small values of height and at most ∼4.5−12° for larger values. The deviation in θ and ϕ increases with height as a consequence of the nonlinear dependence of the two angles on height; specifically, if we examine Figures 8 and 9, we see that both angles increase more rapidly as height is increased for a given aspect ratio. These estimates are consistent with the spread in experimental distributions reported in Figure 6.

IV. Conclusions and Outlook

In this work, we studied flow-induced particle assembly in confined microchannels. We introduced a partially closed membrane valve that is capable of dynamically triggering particle assembly in microchannels. A combination of these valves could potentially be used to meter and transport particles. More importantly, the partially closed membrane valves can be readily integrated with conventional membrane valves (i.e., with hemispherical channel cross-section), allowing regulation of both particle and fluid flow, thus enabling high-throughput synthesis of anisotropic particles.

We investigated packing of spherical particles in confined microchannels and specifically identified anisotropic structures with zigzag morphology. We showed that the bond angles between particle pairs can be controlled by tuning the aspect ratio of the channel geometry. Moreover, we found excellent agreement between experiment, simulation, and theory. The compact theory presented in this work should aid in the design of anisotropic particles.

What does the excellent correspondence between experiment, theory, and simulation suggest about the underlying mechanism governing the formation of these unique structures? Our experimental system consists of non-Brownian particles that undergo flow-driven organization. Our simulations use the method

of Brownian dynamics without hydrodynamics and do not incorporate dynamics due to fluid flow. In addition, our theoretical relationships are derived based on purely geometrical constraints. These observations imply that although flow-induced particle assembly is inherently a nonequilibrium process on these granular scales, the structures we achieve in the range of aspect ratios investigated are essentially equilibrium configurations that are driven by excluded volume interactions (hard-sphere repulsion). In other words, the structures we formed are determined solely by packing constraints and not by Brownian motion, implying that flow-induced assembly can also be used to generate anisotropic structures of smaller length scales comprised of Brownian precursor particles.

In the broader context, what are the potential applications of such close-packed structures generated by 3D confinement? The alternating packing structures generated here are reminiscent of linear polymer chains where the bond angles between monomers (constituent particles) can be designed by tuning the channel dimensions. Current continuous flow methods for anisotropic particle synthesis are not capable of producing such structures. These anisotropic chains could form the building blocks for hierarchical assembly of 3D ordered structures.[40] For example, two or more matching chains with low bond angles could interdigitate; however, chains with high bond angles yield small pockets from which a matching chain will be excluded. Thus, the design rules generated in this work offer control over bond angle variation to build higher order assemblies. In addition, the anisotropic particle chains reported here could be potentially useful for biomolecule analysis, where each constituent particle encodes information for a specific biomolecule and the number of particles in a chain determines the maximum number of biomolecules that can be identified.

Acknowledgment. This study was supported by the National Science Foundation under NSF CBET 0507839 and 0707383. S.C.G. acknowledges support from the Department of Energy under DE-FG02-02ER4600.

LA703840W